





**Vortices of electro-osmotic flow in heterogeneous porous media**Mohammad Mirzadeh <sup>1</sup>, Tingtao Zhou <sup>2</sup>, Mohammad Amin Amooie,<sup>1</sup>  
Dimitrios Fraggedakis <sup>1</sup>, Todd R. Ferguson <sup>3</sup>, and Martin Z. Bazant<sup>1,4,\*</sup><sup>1</sup>*Department of Chemical Engineering, Massachusetts Institute of Technology, Massachusetts 02139, USA*<sup>2</sup>*Department of Physics, Massachusetts Institute of Technology, Massachusetts 02139, USA*<sup>3</sup>*Aramco Americas Company: Aramco Research Center-Boston, 400 Technology Square,  
Cambridge, Massachusetts 02139, USA*<sup>4</sup>*Department of Mathematics, Massachusetts Institute of Technology, Massachusetts 02139, USA*

(Received 15 March 2020; accepted 26 August 2020; published 12 October 2020)

Traditional models of electrokinetic transport in porous media are based on homogenized material properties, which neglect any macroscopic effects of microscopic fluctuations. This perspective is taken not only for convenience but also motivated by the expectation of irrotational electro-osmotic flow, proportional to the electric field, for uniformly charged surfaces (or constant  $\zeta$  potential) in the limit of thin double layers. Here, we show that the inherent heterogeneity of porous media generally leads to macroscopic vortex patterns, which have important implications for convective transport and mixing. These vortical flows originate due to competition between pressure-driven and electro-osmotic flows, and their sizes are characterized by the correlation length of heterogeneity in permeability or surface charge. The appearance of vortices is controlled by a single dimensionless control parameter, defined as the ratio of a typical electro-osmotic velocity to the total mean velocity.

DOI: [10.1103/PhysRevFluids.5.103701](https://doi.org/10.1103/PhysRevFluids.5.103701)**I. INTRODUCTION**

Flows in porous media are everywhere around us [1]. From the small scale of nutrient and heat transport in biological tissues [2] to the geological scale of subsurface flows [3], involved transport processes share common principles. Many transport processes in porous media can be recast in terms of driving forces and corresponding fluxes. This idea is at the heart of nonequilibrium thermodynamics, in which fluxes and driving forces are coupled through Onsager relations that enforce symmetry of the linear response matrix [4]. The nonlinear coupling between various driving forces can result in rich, and sometimes unexpected, behavior. Indeed, recent works indicate electrokinetic phenomena in porous media could be exploited to control viscous fingering [5,6], suppress instabilities in the growth of nanowires [7,8] and porous electrodeposits [9], and drive over-limiting current [10,11] and deionization shock waves [12–14], which enable water purification by shock electrodialysis [15–20].

A unique aspect of transport in porous media is the role of randomness in the pore geometry and network topology [3]. A familiar example is flow channeling in a heterogeneous medium. When subjected to pressure gradient, fluids preferentially flow along the path of least resistance and avoid regions of low permeability, leading to the formation of “flow channels.” Similarly, in two-phase flows, randomness leads to the formation of two well-known phenomena, i.e., the viscous fingering and capillary fingering [21,22]. These instabilities can increase mixing and are

\*bazant@mit.edu

often deemed undesired, e.g., in secondary oil recovery [23]. Quantifying mixing in porous media is also critical to understanding reactive transport [24,25], as well as dissolution trapping in pore fluid following geologic CO<sub>2</sub> sequestration [26,27].

“Passive” control of fluid flow is possible via careful geometrical manipulation, e.g., in patterned micro-fluidic devices to enhance mixing [28,29], or in Hele-Shaw cells [30] and porous media [31] to suppress interfacial instabilities. In passive control, the extent of flow manipulation is limited and difficult to adjust externally or dynamically. Conversely, “active” control may be possible by exploiting the coupling between competing driving forces. One possibility is using electric fields to manipulate fluid flow via electrokinetic phenomena [32]. This idea was recently shown to enable the active control of viscous fingering [5,6] by modifying the effective hydraulic resistance experienced by the fluids.

Traditional models of electro-osmosis in porous media and micro-fluidic devices assume irrotational flow with strongly screened hydrodynamic interactions [33], based on formal homogenization [34] or the mathematical limit of thin double layers and uniform  $\zeta$  potential, in which the fluid velocity is proportional to the (irrotational) electric field [35,36]. Indeed, the assumption of uniform electro-osmotic flow driven by a uniform electric field underlies models of various industrial processes, such as electrokinetic soil remediation and ionic separations [37–41]. Even in situations of stochastic electrotransport with fluctuating electric fields [42], used to accelerate chemical transport for the imaging of biological tissues and organs [43–45], the instantaneous velocity field is assumed to be spatially uniform. The limit of thin double layers is also invoked to justify the approximate independence of electrophoretic mobility on particle shape [46–49], which makes particle separation challenging, unless symmetry is broken by nonuniform [50,51] or induced [52,53] surface charge. Inhomogeneity in surface charge or shape can further be utilized for steady pumping [54,55] or patterning flow fields in microfluidic devices [56,57]. Recently, similar ideas have been proposed for patterning flow fields in Hele-Shaw cells and microfluidic devices using gate electrodes [58–60], although such a strategy would be difficult to achieve in a porous medium.

Here, we demonstrate that a heterogeneous permeability field has a similar effect on patterning the flow field and creating vortical flows, which are beneficial for enhanced mixing. This phenomenon occurs due to strong internal pressure generated by the electro-osmotic flow. Although the concept of electro-osmotic flow reversal is understood for individual pores [32], here we demonstrate similar patterns at the much larger macroscopic scale. Through detailed analyses, we show that the size of vortical structures directly scale with the length scale of heterogeneity in the domain. More importantly, we find that the structure of flow field can be described in terms of the “electro-osmotic coupling coefficient,” a nondimensional parameter measuring the relative strength of electro-osmotic velocity to total mean velocity and which is tunable experimentally. Finally, recent work on coupled nonlinear electrokinetics in random pore network also demonstrate similar vortical flow structures and their interactions with deionization shock waves [61]. In this article, we neglect nonlinear effects and instead provide a clear physical explanation for the formation of vortical structures.

## II. PHYSICAL PICTURE

### A. Electrokinetic phenomena and electro-osmotic pumping

When charged surfaces are brought in contact with an electrolyte solution, a diffuse cloud of ions, namely, the electric double layer (EDL), is formed which screens the surface charge. The EDL is characterized by its thickness, the Debye length ( $\lambda_D$ ), which, for a binary electrolyte, is

$$\lambda_D = \sqrt{\frac{\epsilon k_B T}{2c_0 z^2 e^2}}. \quad (1)$$

Here,  $\epsilon$  is the permittivity of the electrolyte,  $k_B$  is the Boltzmann constant,  $T$  is the absolute temperature,  $c_0$  is the salt concentration,  $z$  is the ion valence, and  $e$  is the elementary charge. Despite

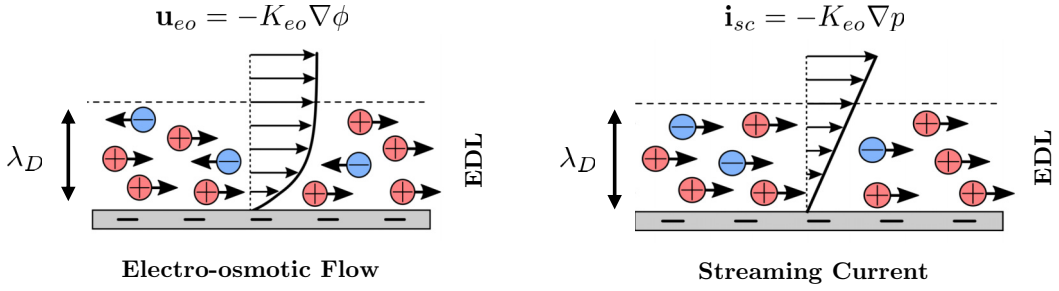


FIG. 1. Many surfaces are charged in aqueous solution. When ions are present in the solution, a thin cloud of mostly counter-ions accumulate near the surface to screen the surface charge and form the electric double layer (EDL). Left: An electric field drives electro-osmotic flow due to electrostatic force on the ions in the EDL. Right: Conversely, streaming current occurs due to advection of charges in the EDL by the pressure-driven flow.

being very thin, the interactions between the ions and solvent molecules in the EDL lead to a myriad of processes that are collectively termed “electrokinetic phenomena” [32] (see Fig. 1). An external electric field parallel to the surface drives “electro-osmotic flow,” with a far-field velocity which, for small driving forces, scales linearly with the electric field  $\mathbf{E} = -\nabla\phi$ :

$$\mathbf{u}_{eo} = K_{eo} \mathbf{E} = -K_{eo} \nabla \phi. \quad (2)$$

Here,  $\phi$  is the electrical potential and  $K_{eo}$  is the electro-osmotic mobility. Similarly, advection of ions in the EDL due to pressure-driven flow generates “streaming current,” with an area-average current density  $\mathbf{i}_{sc} = -K_{sc} \nabla p$ . When the driving forces are small, the Onsager symmetry requires that electrokinetic phenomena are symmetric with respect to driving forces, i.e.,  $K_{sc} = K_{eo}$  [4]. For thin EDL, e.g., compared to the pore size in a porous medium or the gap size in a Hele-Shaw cell, the electro-osmotic mobility is given by the Helmholtz-Smoluchowski relation:

$$K_{eo} = \frac{-\varepsilon \zeta}{\mu}, \quad (3)$$

where  $\mu$  is the electrolyte viscosity and  $\zeta$  is the potential difference across the EDL, which for many surfaces varies in the range of  $-100 < \zeta < 50$  mV at room temperature [32,62].

When both pressure gradients and electric fields are present, the total velocity is the sum of pressure-driven and electro-osmotic components,

$$\mathbf{u} = \mathbf{u}_h + \mathbf{u}_{eo} = -K_h \nabla p - K_{eo} \nabla \phi, \quad (4)$$

where the hydraulic conductivity is given by the Darcy relation,  $K_h = k/\mu$ , and  $k$  is the Darcy permeability. Equation (4) could be understood as the macroscopic velocity in a porous medium, the area-averaged velocity in a cylindrical pore, or the depth-averaged velocity in a Hele-Shaw cell. When electro-osmotic flows are driven into tight pores, strong adverse pressure gradients are generated if the pore cannot sustain the flow rate. This is a consequence of different scaling of pressure-driven and electro-osmotic velocities with the characteristic length-scale  $h \sim \sqrt{k}$ . While the electro-osmotic velocity is independent of geometrical length-scales, the pressure-driven velocity scales quadratically,  $U_h \sim h^2$ . From Eqs. (3) and (4), the maximum pressure gradient occurs when the total velocity is zero, e.g., in a dead-end pore,

$$\Delta p_{eo} \sim \frac{\varepsilon \zeta}{h^2} \Delta \phi. \quad (5)$$

Equation (5) indicates that electro-osmotic flow can “pump” the fluid in the opposite direction of pressure gradient. It is well known that electro-osmotic pumping leads to flow reversal in a dead-end pore or near a bottle-neck [63], which is a possible mechanism for sustaining over-limiting currents

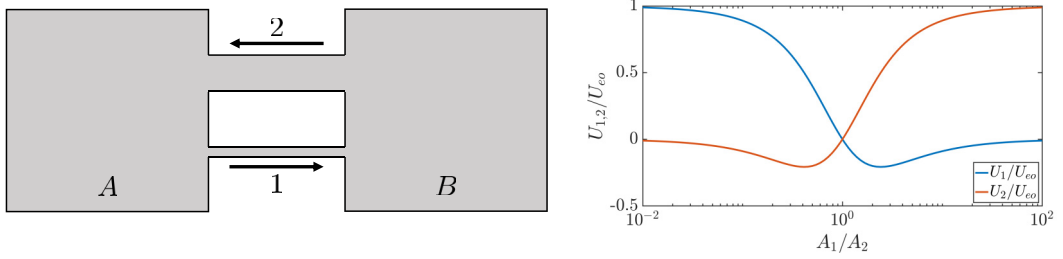


FIG. 2. Flow reversal occurs when pressure-driven and electro-osmotic flows compete. Left: Schematic of two reservoirs “A” and “B,” connected via two parallel “pores” of different sizes  $A_1$  and  $A_2$ . Right: When an electric field is applied from reservoir “A” to “B,” electro-osmotic flow creates an adverse pressure gradient, which drives backward pressure-driven flow. Because the hydraulic and electro-osmotic conductivities scale differently with the pore size, the flow in the smaller pore is always in the opposite direction of the larger pore, leading to a net circulation.

[10,11]. Adverse pressure gradient and internal flow re-circulation also limit the performance of electro-osmotic pumping, which must be circumvented to achieve fast pumping [64–66]. Consider a hypothetical situation where two reservoirs, “A” and “B,” are connected via a small and large pore placed in parallel (see Fig. 2). If an electric field is applied from reservoir “A” to “B,” the electro-osmotic flow creates an adverse pressure difference,

$$\Delta p_{eo} = p_B - p_A = \frac{R_1 R_2}{R_1 + R_2} U_{eo} (A_1 + A_2), \quad (6)$$

where  $A_{1,2}$  and  $R_{1,2}$  are the cross-sectional area and hydraulic resistance of the pores, respectively. This pressure difference drives fluid flow in both pores that are in the opposite direction of electro-osmotic flow, leading to the total area-averaged velocities given by

$$U_1 = U_{eo} - \frac{\Delta p_{eo}}{R_1 A_1} = U_{eo} \left( 1 - \frac{R_2}{R_1 + R_2} \frac{A_1 + A_2}{A_1} \right), \quad (7)$$

$$U_2 = U_{eo} - \frac{\Delta p_{eo}}{R_2 A_2} = U_{eo} \left( 1 - \frac{R_1}{R_1 + R_2} \frac{A_1 + A_2}{A_2} \right). \quad (8)$$

From Darcy’s law,  $R_2/R_1 = (A_1/A_2)^2$ , and therefore the area-averaged velocities may be expressed in terms of relative pore size,  $A_1/A_2$ . Figure 2 illustrates that the average velocity in the larger pore is always in the opposite direction of the smaller pore. This is easy to understand in the limit when  $A_1 \ll A_2$ . In this case, the electro-osmotic flow primarily reverses through the pore with least hydraulic resistance (larger area). The simple analysis presented here is the basis of flow reversal and circulation in a random porous medium as will be shown in the following section. A porous medium with a heterogeneous permeability field may be idealized using a collection of different-sized pores that are connected in series and parallel. While series connection can lead to flow reversal at the pore scale, it is the size variation between parallel pores that lead to flow reversal at the macroscopic level.

It is well known that pore network connectivity impacts fluid flow [22,67,68], ion transport [69], and electrokinetics [61,70] in porous media. Recently, the concept of “accessivity” [71] was introduced to characterize the role of pore network connectivity in explaining the origins of capillary hysteresis in porous media. This concept has also been used to quantify the impact of network heterogeneity on sustaining over-limiting currents through ion-selective membranes [61]. Therefore, it should not be surprising that pore network connectivity also impacts vortex formation. As we shall see, the circulation region in a heterogeneous porous medium roughly scales with the size of heterogeneity, i.e., the length-scale over which the permeability field changes in the domain.

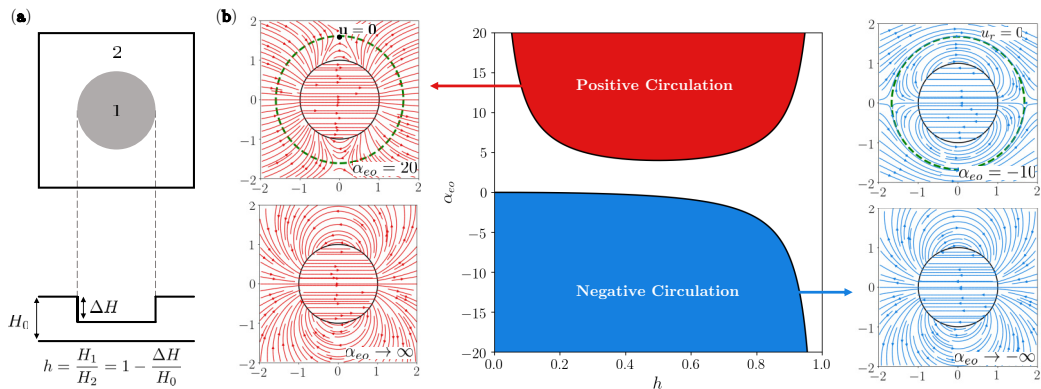


FIG. 3. Flow characterization in a Hele-Shaw cell of variable gap. (a) Schematic of a Hele-Shaw cell with a nonuniform gap. We use “1” and “2” subscripts to refer to parameter and variables defined in each sub-domain. (b) Center: The state of flow field is fully determined by two parameters: the gap ratio,  $h$ , and the electro-osmotic coupling coefficient,  $\alpha_{eo}$ . For any gap ratio, circulation is possible if the electro-osmotic velocity is sufficiently strong. The direction of electro-osmotic flow, denoted by the sign of  $\alpha_{eo}$ , dictates the direction of the dipolar flow field and the sign of circulation. (b) Left, Right: Representative examples of the flow field for the gap ratio of  $h = 0.1$ . The green dashed line represents the extent of circulation region given via Eqs. (25) and (26), which grows in an unbounded fashion as  $|\alpha_{eo}| \rightarrow \infty$ .

However, before turning to porous media, we will first consider a simpler problem in a Hele-Shaw cell with nonuniform gap thickness which allows for analytical solution.

### B. Nonuniform Hele-Shaw cell

Flows in Hele-Shaw cells have been traditionally studied as a two-dimensional idealization of more complex flows in porous media. Moreover, flows in Hele-Shaw cells are considerably easier to visualize experimentally. Recently, several works have shown that by controlling the  $\zeta$  potential through gate electrodes, it is possible to control flow patterns in a uniform Hele-Shaw cell [58–60]. These experiments clearly illustrate the formation of circulation regions around gate electrodes. Here, we consider a Hele-Shaw cell with a disk-like region of narrower gap thickness, but constant  $\zeta$  potential (see Fig. 3). As we will see, the depth-averaged velocity for this problem also exhibits similar circulating flow pattern around the disk region.

We assume a Hele-Shaw cell with a variable gap thickness  $H(\mathbf{x}) = H_0 - \Delta H \chi(\mathbf{x})$ , where  $\chi = 1$  inside the disk of radius  $a$  and  $\chi = 0$  outside. Note that, throughout this articles, lowercase boldface symbols represent vector quantities, e.g.,  $\mathbf{x} = (x, y)$  represents a point in two dimensions. The Hele-Shaw cell is subjected to uniform fluid flow and electric current far away from the disk. The presence of the nonuniformity in the gap thickness affects the hydraulic and electrical resistance near the disk and perturbs the pressure and electric potential fields. To obtain the depth-averaged velocity, we must first solve for the electric potential which satisfies the depth-averaged Ohm’s law,

$$\nabla \cdot [H(\mathbf{x})\sigma \nabla \phi] = 0. \quad (9)$$

Here,  $\sigma$  is the electrolyte conductivity which is assumed to be uniform. Notice that we have ignored the contribution from streaming current in Eq. (9). This assumption is justified for Hele-Shaw cells in which the gap thickness is considerably larger than the Debye length ( $H \gg \lambda_D$ ). We will further comment on this assumption in the next section where we define a nondimensional parameter to quantify the strength of streaming current. The solution to Eq. (9) in polar

coordinates is

$$\phi_1 = -E_\infty r \cos \theta \left( \frac{2}{1+h} \right), \quad (10)$$

$$\phi_2 = -E_\infty r \cos \theta \left( 1 + \frac{a^2}{r^2} \frac{1-h}{1+h} \right), \quad (11)$$

where  $E_\infty$  is the far-field electric field,  $h = H_1/H_2$  is the gap nonuniformity parameter, and  $\phi_1$  and  $\phi_2$  are the solution inside and outside the disk, respectively. Using this solution, the electro-osmotic velocity is given by

$$\mathbf{u}_{\text{eo}}^1 = \frac{2U_{\text{eo}}}{1+h} (\cos \theta \hat{\mathbf{e}}_r - \sin \theta \hat{\mathbf{e}}_\theta), \quad (12)$$

$$\mathbf{u}_{\text{eo}}^2 = U_{\text{eo}} \cos \theta \left( 1 - \frac{a^2}{r^2} \frac{1-h}{1+h} \right) \hat{\mathbf{e}}_r - U_{\text{eo}} \sin \theta \left( 1 + \frac{a^2}{r^2} \frac{1-h}{1+h} \right) \hat{\mathbf{e}}_\theta, \quad (13)$$

where  $U_{\text{eo}} = K_{\text{eo}} E_\infty$  is the uniform far-field electro-osmotic velocity.

For a Hele-Shaw cell, Eq. (4) gives the total depth-averaged velocity with  $k(\mathbf{x}) = H(x)^2/12\mu$ . Mass conservation then requires that

$$\nabla \cdot \left[ \frac{H(\mathbf{x})^3}{12\mu} \nabla p \right] + \nabla \cdot [H(\mathbf{x}) K_{\text{eo}} \nabla \phi] = 0, \quad (14)$$

which combined with Eq. (9) further simplifies to

$$\nabla \cdot \left[ \frac{H(\mathbf{x})^3}{12\mu} \nabla p \right] = 0. \quad (15)$$

Note that the apparent decoupling between the pressure and potential fields in Eq. (15) is simply a result of assuming uniform electro-osmotic mobility and electric conductivity. As we will discuss in the next section, this assumption may not hold in general. Nevertheless, the coupling between the two fields is still enforced through the boundary conditions. The solution to Eq. (15), subject to uniform far-field velocity, is given by

$$p_1 = -\frac{12\mu U_h}{H_0^2} r \cos \theta \left( \frac{2}{1+h^3} \right), \quad (16)$$

$$p_2 = -\frac{12\mu U_h}{H_0^2} r \cos \theta \left( 1 + \frac{a^2}{r^2} \frac{1-h^3}{1+h^3} \right), \quad (17)$$

where  $U_h = U - U_{\text{eo}}$  is the pressure-driven part of the uniform far-field velocity,  $U$ . From Eqs. (16) and (17), the pressure-driven velocity is found as

$$\mathbf{u}_h^1 = \frac{2h^2 U_h}{1+h^3} (\cos \theta \hat{\mathbf{e}}_r - \sin \theta \hat{\mathbf{e}}_\theta), \quad (18)$$

$$\mathbf{u}_h^2 = U_h \cos \theta \left( 1 - \frac{a^2}{r^2} \frac{1-h^3}{1+h^3} \right) \hat{\mathbf{e}}_r - U_h \sin \theta \left( 1 + \frac{a^2}{r^2} \frac{1-h^3}{1+h^3} \right) \hat{\mathbf{e}}_\theta. \quad (19)$$

Finally, the total velocity is

$$\mathbf{u}_{1,2} = \mathbf{u}_h^{1,2} + \mathbf{u}_{\text{eo}}^{1,2}. \quad (20)$$

The velocity field in Eq. (20) is the sum of a uniform background flow and a dipole-like term due to nonuniformity in the gap thickness. This velocity field depends on two nondimensional parameters: the ratio of the gap thickness between inside and outside  $h = H_1/H_2$ , and the ‘‘electro-osmotic coupling coefficient,’’

$$\alpha_{\text{eo}} = \frac{U_{\text{eo}}}{U}, \quad (21)$$

which measures the relative strength of electro-osmotic velocity with respect to the total velocity. For a fixed geometry, the electro-osmotic coupling coefficient can be tuned independently and affects the flow field. When  $\alpha_{\text{eo}} > 0$ , the electro-osmotic and far-field velocities are in the same direction, whereas negative values ( $\alpha_{\text{eo}} < 0$ ) indicate opposite directions. Irrespective of the sign of  $\alpha_{\text{eo}}$ , flow reversal is expected when the electro-osmotic velocity is sufficiently strong, as illustrated in Fig. 3. To characterize the flow behavior, we consider the  $\theta$  component of the total velocity along  $\theta = \pi/2$ ,

$$\frac{u_1(r)}{U} = 2 \left( \frac{\alpha_{\text{eo}}}{1+h} + \frac{(1-\alpha_{\text{eo}})h^2}{1+h^3} \right), \quad r < a, \quad (22)$$

$$\frac{u_2(r)}{U} = 1 + \frac{a^2}{r^2} \left( \alpha_{\text{eo}} \frac{1-h}{1+h} + (1-\alpha_{\text{eo}}) \frac{1-h^3}{1+h^3} \right), \quad r > a. \quad (23)$$

We detect the presence of circulation if  $u_1(a)u_2(a) < 0$ , i.e., the  $\theta$ -component of velocity switches sign across the disk region. Figure 3 illustrates the regions in the  $(h, \alpha_{\text{eo}})$  phase space for which flow circulation is possible,

$$\text{circulation possible: } \alpha_{\text{eo}} \leq \frac{-h^2}{1-h} \quad \text{or} \quad \alpha_{\text{eo}} \geq \frac{1}{h(1-h)}. \quad (24)$$

Note that when  $\alpha_{\text{eo}} > 0$ , the direction of the dipolar flow field is aligned with the pressure-driven flow and we say the circulation is “positive.” Conversely, when  $\alpha_{\text{eo}} < 0$ , the dipolar and pressure-driven flow fields are in the opposite direction and we call the circulation to be “negative.” The extent of the circulation region is computed by requiring that only the radial (when  $\alpha_{\text{eo}} < 0$ ) or both components (when  $\alpha_{\text{eo}} > 0$ ) of velocity are zero at  $(r, \pi/2)$ ,

$$\frac{r}{a} = \sqrt{\frac{1-h^3}{1+h^3} - 2\alpha_{\text{eo}} \frac{h(1-h)}{1+h^3}}, \quad \alpha_{\text{eo}} < \frac{-h^2}{1-h}, \quad (25)$$

$$\frac{r}{a} = \sqrt{2\alpha_{\text{eo}} \frac{h(1-h)}{1+h^3} - \frac{1-h^3}{1+h^3}}, \quad \alpha_{\text{eo}} > \frac{1}{h(1-h)}. \quad (26)$$

Here, we have shown that electro-osmotic flows can generate circulating regions in a Hele-Shaw cell with a nonuniform gap thickness. Although the analysis was more involved than the previous section, the fundamental physical picture remains unchanged: electro-osmotic flows create adverse pressure gradient, which subsequently drive pressure-driven flows in the opposite direction. This can lead to flow reversal and circulation in regions where the gap thickness is nonuniform. The spatial extent of this circulating region scales linearly with the size of nonuniformity.

### III. ELECTROKINETIC TRANSPORT IN RANDOM POROUS MEDIA

#### A. Electrokinetic transport in porous media

The fully coupled electrokinetic transport equations describe a linear relationship between macroscopic, volume-averaged fluxes, i.e., fluid velocity,  $\mathbf{u}$ , and electric current density,  $\mathbf{i}$ , and thermodynamic driving forces, i.e., pressure,  $p$ , and electric potential,  $\phi$  [1,4]. Combined with statements of mass and charge conservation, the governing equations read

$$\nabla \cdot \mathbf{F} = \mathbf{0}, \quad \mathbf{F} = -\mathbb{K} \nabla \Phi, \quad (27)$$

where we use  $\mathbf{F} = (\mathbf{u}, \mathbf{i})^\top$  and  $\Phi = (p, \phi)^\top$  notation for brevity and  $\mathbb{K}$  is the electrokinetic coupling tensor:

$$\mathbb{K} = \begin{pmatrix} K_h & K_{\text{eo}} \\ K_{\text{eo}} & K_e \end{pmatrix}. \quad (28)$$

Equation (27) indicates that the macroscopic fluid velocity is the sum of pressure-driven,  $\mathbf{u}_h = -K_h \nabla p$ , and electro-osmotic,  $\mathbf{u}_{eo} = -K_{eo} \nabla \phi$ , terms. Similarly, the macroscopic electric current density is the sum of Ohmic,  $\mathbf{i}_e = -K_e \nabla \phi$ , and streaming current,  $\mathbf{i}_{sc} = -K_{eo} \nabla p$ , terms. The symmetry of the electrokinetic tensor,  $\mathbb{K}$ , is a result of microscopic reversibility and can be directly verified using Stokes and Poisson-Nernst-Planck equations [4,72]. Here,  $K_h(\mathbf{x}) = k(\mathbf{x})/\mu$  is the hydraulic conductivity, where  $k(\mathbf{x})$  denotes the permeability coefficient at a point  $\mathbf{x} = (x, y)$ . As discussed later, we use Gaussian random fields to generate the permeability coefficient from a known autocorrelation function to simulate the effects of heterogeneity on the electrokinetic response.

In this article, we focus on linear electrokinetics and thin EDL approximation. Therefore, we express the macroscopic electrokinetic mobility,  $K_{eo}$ , according to the Helmholtz-Smoluchowski relation,  $K_{eo} = -\varepsilon \zeta / \mu$ . Here,  $\zeta$  may be interpreted as a macroscopically averaged surface potential for the entire porous medium and assumed to be uniform [72–74]. The macroscopic electrical conductivity,  $K_e$ , is related to the electrolyte conductivity,  $\sigma$ , through  $K_e = \sigma \varepsilon / \tau$ , where  $\varepsilon$  and  $\tau$  are the porosity and tortuosity coefficients, respectively [75,76]. Here, we have ignored effects of surface conductivity [69], which is consistent with the assumption of linear electrokinetic response. Furthermore, we assume the macroscopic electrical conductivity to be uniform. This assumption is justified for a porous medium with uniform  $\tau/\varepsilon$  ratio, the so-called “formation factor” [1,77], and saturated with an electrolyte of uniform concentration. More realistically, both the electro-osmotic and electrical conductivities could be nonuniform in the medium. Variations in surface charge density, electrolyte concentration, or formation factor can all lead to a complex, and possibly dynamic, electrokinetic response such as propagation of deionization shock waves [13,61]. In this article, we only consider heterogeneity in the permeability coefficient to focus on basic ideas. As we will see, even the simple linear model can lead to rich and chaotic fluid behavior.

The strength of electrokinetic coupling is measured in terms of the nondimensional coupling coefficient:

$$\alpha = \frac{K_{eo}^2}{K_h K_e}, \quad (29)$$

which also controls the efficiency of electrokinetic energy conversion [78]. The second law of thermodynamic requires that  $0 \leq \alpha < 1$  ( $\det \mathbb{K} \geq 0$ ). In the limit of thin EDLs, the coupling is typically weak, i.e.,  $\alpha \ll 1$ . In this “weak coupling” limit, only the streaming current or electro-osmotic flow can be large but not both at the same. This can be verified by introducing two nondimensional parameters:

$$\alpha_{eo} = \frac{K_{eo} I}{K_e U} \sim U_{eo}/U, \quad \alpha_{sc} = \frac{K_{eo} U}{K_h I} \sim I_{sc}/I, \quad (30)$$

which measure the relative importance of electro-osmotic velocity and streaming current, respectively. By comparing to Eq. (29), it is clear that  $\alpha = \alpha_{eo} \alpha_{sc}$  and therefore, in the limit of weak coupling, both effects cannot be strong at the same time.

In our numerical simulations, we solve the fully coupled Eqs. (27). However, to better understand the role of electro-osmotic flow, we can simplify these equations in the limit of weak streaming current, i.e.,  $\alpha_{sc} \ll 1$ :

$$\nabla \cdot [K_h(\mathbf{x}) \nabla p] + K_{eo} \nabla^2 \phi = 0, \quad (31)$$

$$K_e \nabla^2 \phi = 0. \quad (32)$$

Equation (31) can further be simplified by using Eq. (32):

$$\nabla \cdot \left[ \frac{k(\mathbf{x})}{\mu} \nabla p \right] = 0, \quad (33)$$

$$\nabla^2 \phi = 0. \quad (34)$$



The apparent decoupling of pressure and potential fields is again due to assuming uniform electrokinetic and electric conductivity coefficients. As discussed earlier, and more realistically, all of the terms in the conductivity tensor in Eq. (28) could be heterogeneous, leading to fully coupled system of equations. Variation in the  $\zeta$  potential is possible due to heterogeneous surface chemistry. Furthermore, spatiotemporal variations in the electrolyte properties, such as pH and salt concentration, can lead to nonlinear electrokinetic response and formation of deionization shocks, which cause heterogeneous  $\zeta$  potential and solution conductivity [61]. Nevertheless, the pressure and electric potential are still coupled through the boundary conditions when fluxes are prescribed:

$$-\frac{k(\mathbf{x})}{\mu} \hat{\mathbf{n}} \cdot \nabla p = U_n + K_{\text{eo}} \hat{\mathbf{n}} \cdot \nabla \phi, \quad (35)$$

$$-K_e \hat{\mathbf{n}} \cdot \nabla \phi = I_n, \quad (36)$$

where  $\hat{\mathbf{n}}$  denotes the normal to the boundary, and  $U_n$  and  $I_n$  are the total velocity and electric current density, respectively. Here, the term ‘‘boundary’’ refers to the side boundary of the computational domain (see Sec. III C). Combining Eqs. (35) and (36) yields the following simple boundary condition for the pressure:

$$-\frac{k(\mathbf{x})}{\mu} \hat{\mathbf{n}} \cdot \nabla p = U_n - \frac{K_{\text{eo}}}{K_e} I_n = U_n(1 - \alpha_{\text{eo}}). \quad (37)$$

Equation (37) suggests that the pressure field and fluid velocity can be directly controlled by adjusting the current density at the boundaries. Finally, once the pressure and electric potential are known, the fluid velocity in the domain is given via

$$\mathbf{u} = -\frac{k(\mathbf{x})}{\mu} \nabla p - K_{\text{eo}} \nabla \phi = (1 - \alpha_{\text{eo}}) \mathbf{u}_0 + \mathbf{u}_{\text{eo}}, \quad (38)$$

where  $\mathbf{u}_0$  is the fluid velocity for the same problem but at zero electric field and  $\mathbf{u}_{\text{eo}} = -K_{\text{eo}} \nabla \phi$ . Because  $\alpha_{\text{eo}}$  is controlled by the electric current, it can be tuned independent of the fluid velocity. Remarkably, when  $\alpha_{\text{eo}} = 1$ , the fluid velocity is independent of pressure field and is entirely dictated by the electro-osmotic velocity.

## B. Random field generation

We use random fields to represent heterogeneous properties in a random porous medium. Specifically, we assume the permeability field is given via

$$k(\mathbf{x}) = k_0 \exp[z(\mathbf{x})], \quad (39)$$

where  $k_0$  is a reference value and  $z(\mathbf{x})$  is a random field with a known autocorrelation function  $\xi(\mathbf{x})$ :

$$\xi(\mathbf{x}) = \int z(\mathbf{x}') z(\mathbf{x}' - \mathbf{x}) d\mathbf{x}', \quad (40)$$

We further assume the random field  $z(\mathbf{x})$  to be statistically isotropic, i.e.,  $\xi(\mathbf{x}) = \xi(|\mathbf{x}|)$ , although this restriction can be easily lifted. Different correlation functions may be assumed depending on the statistical properties of the medium. Here, we assume Gaussian correlations, i.e.,

$$\xi(|\mathbf{x}|) = \xi_0 \exp(-|\mathbf{x}|^2/\ell^2), \quad (41)$$

where  $\xi_0$  controls the variance of the random field  $z(\mathbf{x})$ . Indeed, we have  $\xi_0 = \sigma^2 + \mu^2$  where  $\sigma^2$  and  $\mu$  are the variance and mean of the random field  $z(\mathbf{x})$ . The ‘‘correlation length’’  $\ell$ , defines a length-scale over which the correlations in the random field decay and could be understood as defining a ‘‘feature size’’ in the random field (see Fig. 4).

We use fast Fourier transform (FFT) to generate random fields efficiently. This approach is similar to the algorithm presented by the authors of Refs. [79,80] and based on the Wiener-Khinchin

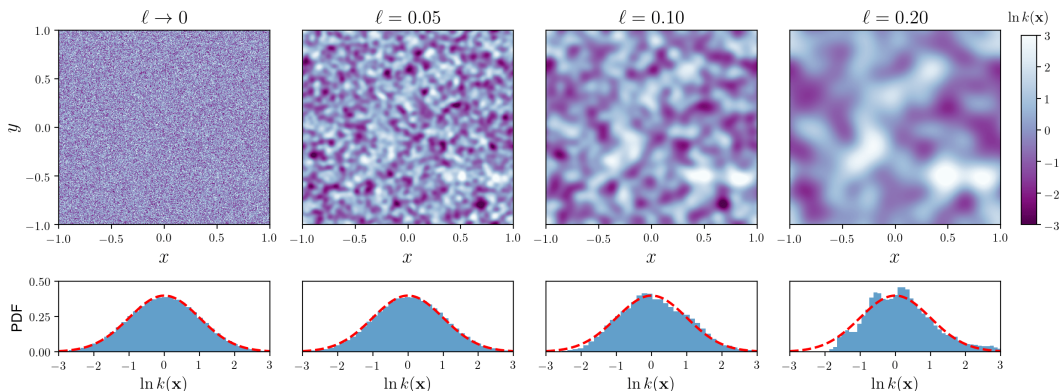


FIG. 4. We use Gaussian random fields to represent heterogeneity in the permeability function  $k(\mathbf{x})$ . Top: A sequence of random fields are generated from a known autocorrelation function [Eq. (41), with  $\xi_0 = 1$ ] with increasing correlation length,  $\ell$ . When  $\ell \rightarrow 0$ , the random field appears as a white noise but increasing the correlation length reduces large variations in nearby points and results in a smoothly varying random field. Bottom: The probability density function (PDF) for the spatial distribution of log-permeability [ $z(\mathbf{x}) = \ln k(\mathbf{x})$ , with  $k_0 = 1$ ]. The red dashed curve is the standard normal distribution. When  $\ell \rightarrow 0$ , the log-permeability function has a normal distribution, as expected. As correlation length becomes larger, the spatial distribution is distorted due to correlations and finite-size effects.

theorem, which states that the autocorrelation and power spectral density functions are Fourier transform pairs,

$$\xi(\mathbf{x}) \stackrel{\mathcal{F}}{\longleftrightarrow} S(\mathbf{k}) : \mathcal{F}\xi(\mathbf{x}) = |\mathcal{F}z(\mathbf{x})|^2 = S(\mathbf{k}), \quad (42)$$

where  $\mathcal{F}$  denotes the Fourier transform and  $\mathbf{k} = (k_x, k_y)$  is the wave vector in two dimensions. For the Gaussian autocorrelation function defined in Eq. (41), the power spectral density is given via

$$S(|\mathbf{k}|) = \int \xi(|\mathbf{x}|) e^{-i\mathbf{k}\cdot\mathbf{x}} d\mathbf{x} = \pi \xi_0 \ell^2 \exp(-\ell^2 |\mathbf{k}|^2 / 4). \quad (43)$$

With a known power spectral density, we generate the random field  $z(\mathbf{x})$  by taking inverse Fourier transform while randomizing the phase of individual modes:

$$z(\mathbf{x}) = \mathcal{F}^{-1}[\sqrt{S(|\mathbf{k}|)} e^{i\theta(\mathbf{k})}] = \frac{1}{4\pi^2} \int \sqrt{S(|\mathbf{k}|)} e^{i\theta(\mathbf{k})} e^{i\mathbf{k}\cdot\mathbf{x}} d\mathbf{k}, \quad (44)$$

where  $\theta(\mathbf{k})$  is the random phase angle for mode  $\mathbf{k}$ , which is drawn from a uniform distribution, i.e.,  $\theta(\mathbf{k}) \sim \mathcal{U}(0, 2\pi)$ . We also require that  $\theta(-\mathbf{k}) = \theta(\mathbf{k})$ , so that  $z(\mathbf{x})$  is real valued. Equation (44) could be understood as a superposition of plane waves with amplitude  $\sqrt{S(|\mathbf{k}|)}$  and randomized phase angles. Alternatively, Eq. (44) could also be understood as smoothing a white noise field using a filter whose power density is  $S(|\mathbf{k}|)$ . Figure 4 illustrates a sequence of random fields generated using Eq. (44) with  $\xi_0 = 1$  and different correlation lengths.

### C. Numerical simulations

We numerically solve the system of Eqs. (27) in nondimensional form. This is achieved by introducing the following nondimensional variables:

$$\hat{\mathbf{x}} = \frac{\mathbf{x}}{L}, \quad \hat{k}(\mathbf{x}) = \frac{k(\mathbf{x})}{k_0}, \quad \hat{p} = \frac{pk_0}{UL\mu}, \quad \hat{\phi} = \frac{\phi K_e}{IL}, \quad \hat{\mathbf{u}} = \frac{\mathbf{u}}{U}, \quad \hat{\mathbf{i}} = \frac{\mathbf{i}}{I}, \quad (45)$$

where  $L$  is a reference macroscopic size,  $k_0$  is a reference permeability coefficient, and  $U$  and  $I$  are reference velocity and electric current density values. For brevity, we will omit the hat notation in the remaining of this article and treat all variables as nondimensional unless otherwise noted. The resulting nondimensional equations are given via

$$\nabla \cdot [k(\mathbf{x})\nabla p] + \alpha_{\text{eo}}\nabla^2\phi = 0, \quad (46)$$

$$\alpha_{\text{sc}}\nabla^2 p + \nabla^2\phi = 0, \quad (47)$$

with the coupling coefficients defined in Eq. (30).

As discussed earlier, the nondimensional coupling coefficient,

$$\alpha = \alpha_{\text{eo}}\alpha_{\text{sc}} = \frac{K_{\text{eo}}^2}{K_e K_h} = \frac{\varepsilon^2 \zeta^2 k_0}{\mu K_e}, \quad (48)$$

measures the overall coupling between pressure and potential field and is often very small in practice. For instance, assuming a reference permeability  $k_0 = 10 \text{ mD} \approx 10^{-14} \text{ m}^2$ , surface potential  $\zeta = -50 \text{ mV}$ , electrical conductivity  $K_e \approx 7.5 \text{ mS m}^{-1}$  and dielectric constant  $\varepsilon \approx 7 \times 10^{-10} \text{ F m}^{-1}$ , the coupling coefficient is  $\alpha \approx 1.6 \times 10^{-2}$ .

As discussed in the previous section, we expect the vortical structures to first appear when  $|\alpha_{\text{eo}}| \sim 1$ . From Eq. (30), this condition corresponds to a critical injection ratio of

$$(I/U)_{\text{cr}} = \frac{K_e}{K_{\text{eo}}} \approx 212 \frac{\text{mA cm}^{-2}}{\text{cm s}^{-1}}. \quad (49)$$

For a velocity of  $U \approx 0.1 \text{ mm s}^{-1}$ , the critical current is relatively small  $I_{\text{cr}} \approx 2.1 \text{ mA cm}^{-2}$ . We also note that the right-hand side of Eq. (49) is reciprocal of an important quantity in the geophysics community, i.e., the ‘‘electrokinetic coupling coefficient,’’  $C = K_{\text{eo}}/K_e$  [81]. This quantity is often determined directly through streaming potential measurements. For many reservoirs, measured values fall in the range of  $C \sim 10^{-9} - 10^{-5} \text{ V Pa}^{-1}$  depending on the pore fluid salinity, with typical value of  $C \approx 10^{-6}$  at salinity level of  $\sim 1 \text{ mM}$  [82].

We solve the coupled Eqs. (46) and (47) in a square domain  $\Omega = [-1, 1]^2$  subjected to prescribed flux values at the left and right boundary,

$$-k(\pm 1, y) \frac{\partial p}{\partial y} \Big|_{x=\pm 1} - \alpha_{\text{eo}} \frac{\partial \phi}{\partial y} \Big|_{x=\pm 1} = 1, \quad (50)$$

$$-\alpha_{\text{sc}} \frac{\partial p}{\partial y} \Big|_{x=\pm 1} - \frac{\partial \phi}{\partial y} \Big|_{x=\pm 1} = 1, \quad (51)$$

and no flux conditions at the top and bottom boundaries. Figure 5 illustrates the formation of vortical structures for different values of electro-osmotic coupling coefficient and correlation length. At zero electro-osmotic coupling, the fluid flow is dictated by the pressure field and the heterogeneous permeability field. As the coupling coefficient is increased, the velocity field initially becomes uniform, assisted by the electro-osmotic flow in the same direction. From Eq. (38), when  $\alpha_{\text{eo}} = 1$ , the flow field is entirely determined by the electro-osmotic component, which is uniform due to uniform electric field. When  $\alpha_{\text{eo}} > 1$ , strong electro-osmotic flows through regions of low permeability create backward pressure-driven flow through regions of high permeability, resulting in a circulating flow field. The size of vortical structures is therefore directly related to the separation distance between low and high permeability values, which is controlled by the correlation length parameter  $\ell$ .

Figure 6 illustrates the flow patterns when the electro-osmotic and pressure driven flows are in the opposite direction. This is simulated by reversing the sign of the electro-osmotic coupling coefficient, which has the same effect as reversing the sign of electric current in boundary condition Eq. (51). Unlike Fig. 5, vortical structures can appear for any value of electro-osmotic coupling, even when  $|\alpha_{\text{eo}}| < 1$ . Nevertheless, the number of vortices grows as the magnitude of electro-osmotic

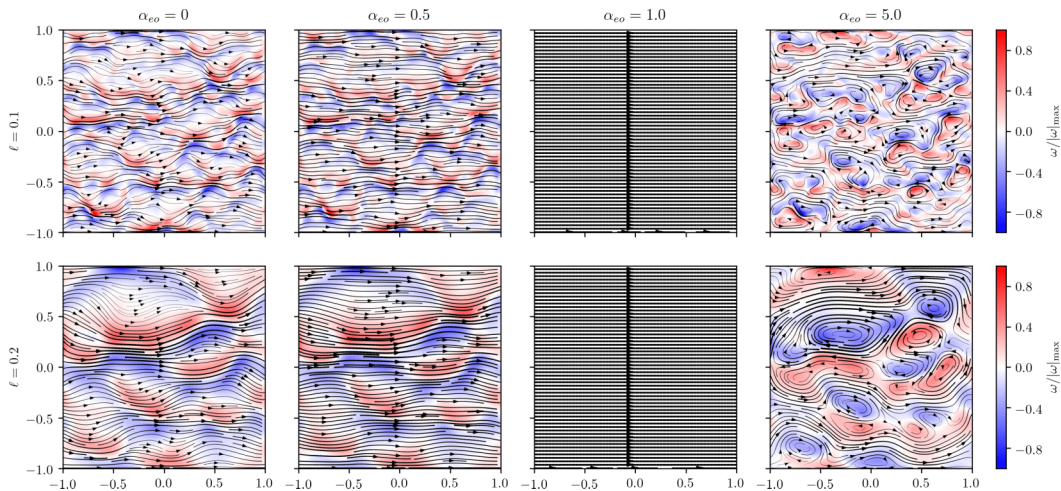


FIG. 5. Effects of electro-osmotic coupling coefficient ( $\alpha_{eo}$ ) and correlation length ( $\ell$ ) on the vortex size. The solid lines are the streamlines and the background color is the normalized vorticity, i.e.,  $\omega/|\omega|_{\max}$ , where  $\omega = \nabla \times \mathbf{u}$  is the fluid vorticity and  $|\omega|_{\max}$  is the maximum absolute value of vorticity in the domain. When  $\alpha_{eo} = 1$ , the flow field is entirely determined by the electro-osmotic flow, which is uniform due to uniform electric field [cf. Eq. (38)].

coupling is increased. These results indicate that vortex generation is a consequence of nonuniform competition between electro-osmotic and pressure driven flows and occurs when electro-osmotic flows are sufficiently strong.

From Figs. 5 and 6, it appears that the vortex size directly scales with the correlation size. To quantify this relationship, we generate different realizations for fixed correlation length and compute the ensemble average number of vortices. We define a vortex center as the maximum or minimum

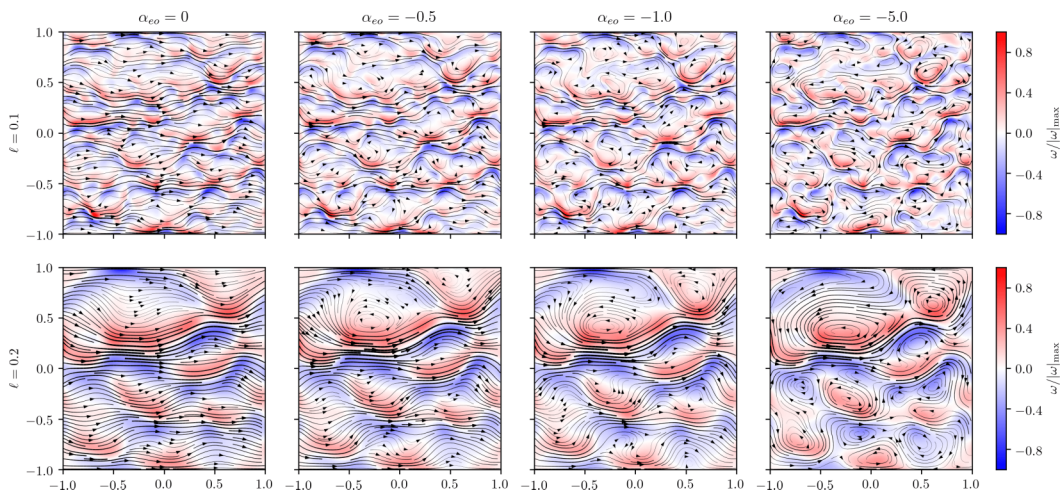


FIG. 6. Vortical structure persist when the electro-osmotic and pressure driven flows are in the opposite directions. The solid lines are the streamlines and the background color is the normalized vorticity, i.e.,  $\omega/|\omega|_{\max}$ , where  $\omega = \nabla \times \mathbf{u}$  is the fluid vorticity and  $|\omega|_{\max}$  is the maximum absolute value of vorticity in the domain. Note that, unlike Fig. 5, the vortical structures appear even when  $|\alpha_{eo}| < 1$ .

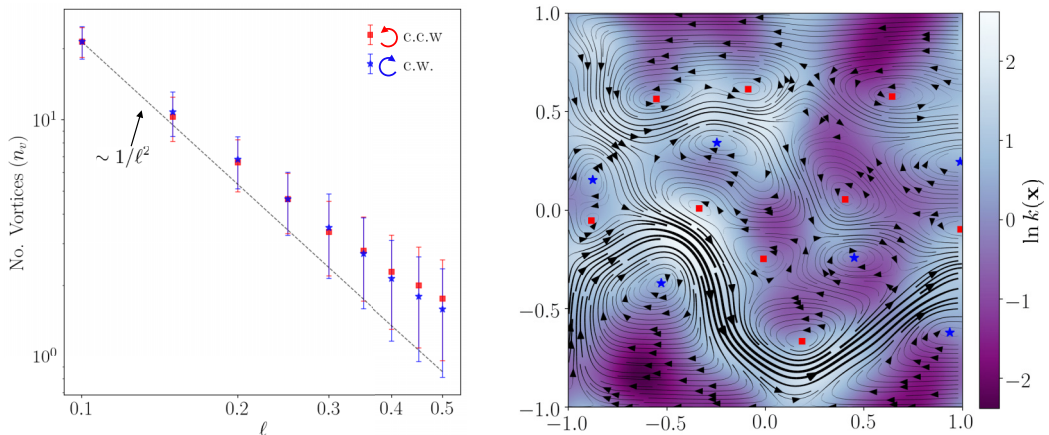


FIG. 7. Statistical analysis of vortex size. Left: The number of vortices (both clockwise and counter-clockwise) increases as the correlation length is decreased and scales as  $n_v \sim \ell^{-2}$  for sufficiently small correlation lengths. The electro-osmotic coupling coefficient was set to  $\alpha_{eo} = -3$ . The symbols represent ensemble averages and error bars are one standard deviation involving 100 simulations for each value of correlation length. The discrepancy at larger correlation length might be due to finite size effects and strong interaction of vortices in the periodic domain. Right: A representative example illustrating the applicability of our algorithm in detecting vortex centers for  $\ell = 0.2$ .

of the stream function,  $\psi$ ,

$$\mathbf{u} = \left( \frac{\partial \psi}{\partial y}, -\frac{\partial \psi}{\partial x} \right)^\top. \quad (52)$$

In this definition, clockwise vortices are associated with the minima of the stream function (negative vorticity) and counterclockwise vortices are associated with the maxima of the stream function (positive vorticity). To detect vortices, first a collection of candidate critical points are selected by thresholding the velocity magnitude, i.e.,  $|\mathbf{u}| < 5 \times 10^{-3} U_{\max}$  where  $U_{\max}$  is the maximum velocity magnitude in the domain. Next, the saddle points are rejected by computing the eigen-values of the Hessian matrix:

$$\mathbf{H} = \begin{pmatrix} \frac{\partial^2 \psi}{\partial x^2} & \frac{\partial^2 \psi}{\partial x \partial y} \\ \frac{\partial^2 \psi}{\partial x \partial y} & \frac{\partial^2 \psi}{\partial y^2} \end{pmatrix}, \quad (53)$$

given via

$$\lambda^2 - \text{tr}(\mathbf{H})\lambda + \det(\mathbf{H}) = 0. \quad (54)$$

The critical points of the stream function are then classified accordingly:

$$\text{maximum} : \lambda_1 > 0, \lambda_2 > 0, \quad \text{minimum} : \lambda_1 < 0, \lambda_2 < 0, \quad \text{saddle} : \lambda_1 \lambda_2 < 0. \quad (55)$$

Figure 7 illustrates the ensemble averaged number of vortices as a function of correlation length. The number of vortices ( $n_v$ ) increases as the correlation size is decreased, and for sufficiently small values, scales as  $n_v \sim \ell^{-2}$ . This scaling further suggests that the average vortex size scales with the correlation length, i.e.,  $l_v \sim 1/\sqrt{n_v} \sim \ell$ . Interestingly, the appearance of adjacent counter-rotating vortices resembles the vortical patterns often observed in “bacterial turbulence” [83]. Similar alternative charge ordering is also observed in the ionic positions of cations and anions in ionic liquids [84]. It would be interesting to see if similar “antiferromagnetic” ordering also applies for

electrokinetic vortices and whether the ideas presented in Ref. [84] can be used to reconstruct the flow field.

#### D. Electrokinetic mixing

We finish this paper by pointing that the ideas presented in this article might be helpful in controlling and enhancing mixing in porous media. Mixing in porous media is important in engineering applications and geological processes such as secondary oil recovery, contaminant transport, and soil and groundwater remediation [24,25]. When reactions are fast, transport processes are diffusion-limited and will benefit from enhanced mixing. Recently, there has been renewed interest in the role of heterogeneity in enhancing the mixing rate [85]. In a heterogeneous media, mixing is improved due to increased velocity fluctuation and material stretching [86,87]. Nevertheless, in passive mixing, it is difficult to control the degree of mixing due to small Reynolds number.

As we have shown in this paper, electrokinetic phenomena can generate strong vortical flows, which are easy to control. Combined with a suitable control strategy, electrokinetic vortices could enhance chaotic mixing in porous media and improve existing remediation techniques [37,38]. Note that our proposed idea is different from chaotic electrokinetic flows in microfluidic channels [88,89] and near ion-selective membranes [90–92], which are generated due to nonlinear interactions. It is also different from stochastic electrotransport in porous media subjected to randomly fluctuating electric fields [42], which are used to deliver and purge chemicals in preparation for imaging of large tissue sample, such as whole mouse brains [43–45], although the dispersion caused by any electrokinetic vortex patterns could ideally be added to effective diffusion coefficient associated with random electrophoretic drift.

To provide a concrete example, consider a rotating electric field defined as

$$\mathbf{E} = E_0[\cos(\omega t), \sin(\omega t)]^T, \quad (56)$$

with constant frequency  $\omega = 2\pi/T$ . For simplicity, we assume the period is equal to the advection timescale, i.e.,  $T = L/U$ . This electric field can be realized by placing two sets of perpendicular electrodes, with AC signals at constant frequency and phase shift of  $\pi/2$ . To obtain the flow field, we solve the nondimensional electrokinetic Eqs. (46). For simplicity, we neglect the effects of streaming current by setting  $\alpha_{sc} = 0$  while the electro-osmotic coupling coefficient is used to control the degree of mixing. Experimentally, this corresponds to adjusting the electric field magnitude  $E_0$  via Eq. (30). The boundary condition for the total velocity is given via Eq. (47), in the  $x$  direction, and no-flux condition in the  $y$  direction, as before. For the electric potential, we instead impose rotating electric fields [Eq. (56)] at the boundaries, which in nondimensional form reads

$$-\frac{\partial\phi}{\partial x}\Big|_{x=\pm 1} = \cos(2\pi t), \quad -\frac{\partial\phi}{\partial y}\Big|_{y=\pm 1} = \sin(2\pi t). \quad (57)$$

Finally, we use correlation length of  $\ell = 0.15$  to generate the permeability function as discussed in Sec. III B.

The rotating electric field generates a periodic unsteady flow field, which can cause strong mixing, especially in applications where the field rotation is stochastic, caused by random motion of a porous sample [42]. We characterize the effectiveness of electro-osmotic mixing via Lagrangian advection of tracers with the local velocity field,

$$\frac{d\mathbf{x}}{dt} = \mathbf{u}(\mathbf{x}, t). \quad (58)$$

Figure 8 illustrates consecutive snapshots of advecting  $N = 50\,000$  tracers during one period of rotating field for different values of electro-osmotic coupling coefficient [93]. The tracers are initially distributed uniformly and randomly inside a disk region and are colored to better demonstrate the mixing process. As the strength of electro-osmotic flow is increased (larger  $\alpha_{eo}$ ), the mixing is enhanced due to stronger vortical flow. Although mixing still occurs without electric field (top row)

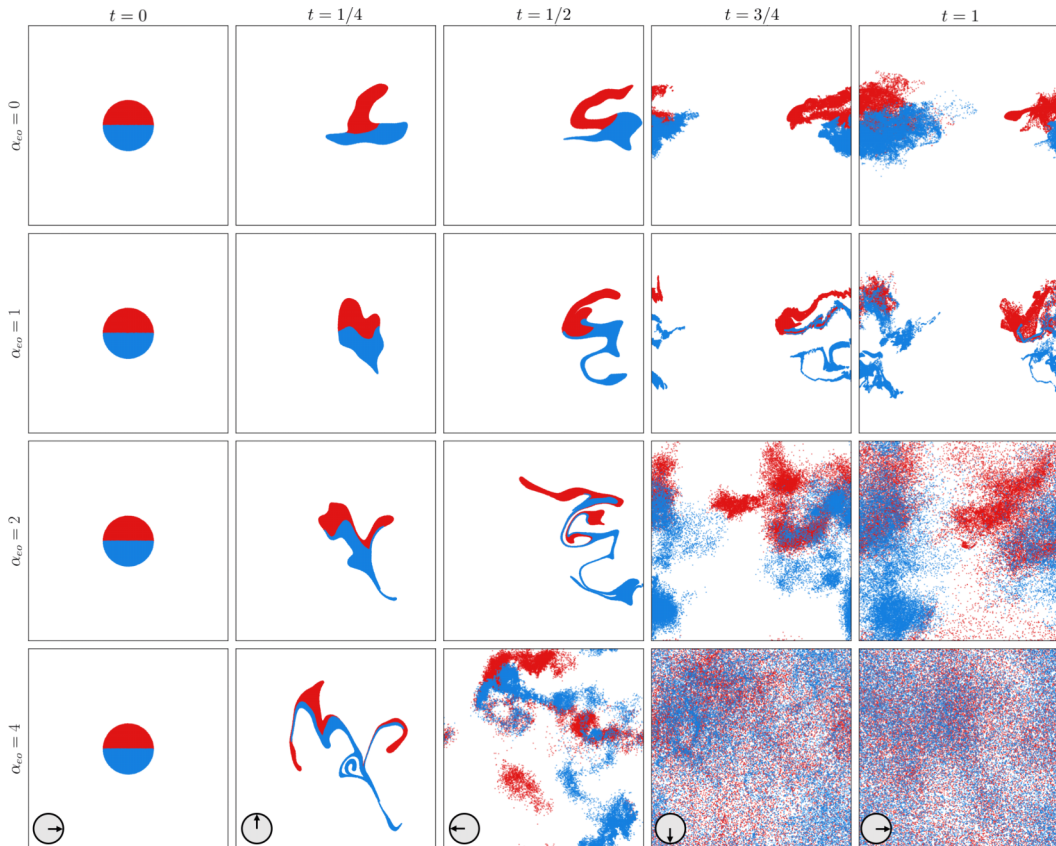


FIG. 8. Effect of electro-osmotic vortices on mixing. A rotating electric field, shown by the small arrow in the last row, generates an unsteady flow field that causes strong mixing. This is demonstrated by advection of 50 000 Lagrangian markers with the local flow field. Mixing is enhanced as the strength of electro-osmotic flow is increased. The background permeability field (omitted for clarity) is the same in all cases and corresponds to a random field with  $\ell = 0.15$ .

due to spatial velocity fluctuations, it is significantly enhanced by the presence of electro-osmotic vortices as evident in the bottom row.

#### IV. CONCLUSIONS

In this article, we have demonstrated that electro-osmotic flows in heterogeneous porous media can lead to the formation of vortex patterns. This phenomenon occurs due to competition between pressure-driven and electro-osmotic flows. Because the pressure-driven and electro-osmotic flows scale differently with the pore size, large internal pressure gradients are created when electro-osmotic flow is pushed through tight pores. When the permeability field is nonuniform, the generated pressure creates backward flow through regions of high permeability. Although this mechanism has been widely known for a single pore, here we demonstrated that a similar flow reversal also occurs on the macroscopic scale, much larger than individual pores. Through detailed analyses, we showed that the spatial extent of vortical structures directly scales with the length scale of the heterogeneity in the permeability field. We also introduce a nondimensional parameter, the electro-osmotic coupling coefficient,  $\alpha_{eo}$ , which describes the relative strength of electro-osmotic flow and controls the flow pattern. When  $\alpha_{eo} \sim 1$ , the electro-osmotic flow is comparable to

pressure-driven flow and vortical structures first appear. Importantly, the electro-osmotic coupling coefficient may be tuned by adjusting the applied current or electric field, independently from the flow rate and pressure difference.

The analysis we have presented here may be extended in several ways. First, we have assumed that only the permeability field is heterogeneous while other material properties are uniform in the domain. In practice,  $\zeta$  potential could also be heterogeneous due to nonuniform chemical composition. Moreover, several material properties could change dynamically with flow field. In single-phase flows, variation in salt concentration or pH can lead to changes in electrolyte conductivity and  $\zeta$  potential, leading to nonlinear coupling and formation of deionization shock waves. The problem is even more complex in two-phase flows, where the immiscibility can lead to unequal partitioning of ions and nonuniform electrokinetic response. Recent works in Hele-Shaw cells suggest these interactions can be exploited to control viscous fingering, but their applicability to porous media is still unknown. Both the nonlinear response and two-phase electrokinetic flow in porous media are novel problems that require further theoretical and experimental investigations.

Finally, we have shown that strong electro-osmotic flows generate vortical structures that promote fluid mixing. Although several mixing strategies have been proposed in microfluidic systems, controllable mixing in porous media is more difficult to achieve. This is because such techniques often rely on geometrical modifications, which are usually not possible in a porous medium. By contrast, electrokinetic mixing relies on the inherent heterogeneity of the medium and is easily controlled externally. The ideas presented in this article may therefore be exploited in applications where controllable mixing is desired, e.g., in enhancing reaction rates in porous electrodes, improving the effective diffusivity of molecules in biological tissues, and diluting contaminants in soil during electrokinetic remediation.

#### ACKNOWLEDGMENTS

This work was supported by a fund from Aramco Americas Company under Contract No. A-0434-2017.

- 
- [1] J. Bear, *Dynamics of Fluids in Porous Media* (Courier Corporation, North Chelmsford, MA, 2013).
  - [2] A.-R. Khaled and K. Vafai, The role of porous media in modeling flow and heat transfer in biological tissues, *Int. J. Heat Mass Transf.* **46**, 4989 (2003).
  - [3] M. Sahimi, *Flow and Transport in Porous Media and Fractured Rock: From Classical Methods to Modern Approaches* (John Wiley & Sons, New York, NY, 2011).
  - [4] S. R. De Groot and P. Mazur, *Non-equilibrium Thermodynamics* (Courier Corporation, North Chelmsford, MA, 2013).
  - [5] M. Mirzadeh and M. Z. Bazant, Electrokinetic Control of Viscous Fingering, *Phys. Rev. Lett.* **119**, 174501 (2017).
  - [6] T. Gao, M. Mirzadeh, P. Bai, K. M. Conforti, and M. Z. Bazant, Active control of viscous fingering using electric fields, *Nat. Commun.* **10**, 4002 (2019).
  - [7] J.-H. Han, E. Khoo, P. Bai, and M. Z. Bazant, Over-limiting current and control of dendritic growth by surface conduction in nanopores, *Sci. Rep.* **4**, 7056 (2014).
  - [8] S. Shin, T. T. Al-Housseiny, B. S. Kim, H. H. Cho, and H. A. Stone, The race of nanowires: Morphological instabilities and a control strategy, *Nano Lett.* **14**, 4395 (2014).
  - [9] J.-H. Han, M. Wang, P. Bai, F. R. Brushett, and M. Z. Bazant, Dendrite suppression by shock electrodeposition in charged porous media, *Sci. Rep.* **6**, 28054 (2016).
  - [10] E. V. Dydek, B. Zaltzman, I. Rubinstein, D. S. Deng, A. Mani, and M. Z. Bazant, Overlimiting Current in a Microchannel, *Phys. Rev. Lett.* **107**, 118301 (2011).



- [11] A. Yaroshchuk, E. Zholkovskiy, S. Pogodin, and V. Baulin, Coupled concentration polarization and electroosmotic circulation near micro/nanointerfaces: Taylor-Aris model of hydrodynamic dispersion and limits of its applicability, *Langmuir* **27**, 11710 (2011).
- [12] T. A. Zangle, A. Mani, and J. G. Santiago, Theory and experiments of concentration polarization and ion focusing at microchannel and nanochannel interfaces, *Chem. Soc. Rev.* **39**, 1014 (2010).
- [13] A. Mani and M. Z. Bazant, Deionization shocks in microstructures, *Phys. Rev. E* **84**, 061504 (2011).
- [14] S. Nam, I. Cho, J. Heo, G. Lim, M. Z. Bazant, D. J. Moon, G. Y. Sung, and S. J. Kim, Experimental Verification of Overlimiting Current by Surface Conduction and Electro-Osmotic Flow in Microchannels, *Phys. Rev. Lett.* **114**, 114501 (2015).
- [15] D. Deng, E. V. Dydek, J.-H. Han, S. Schlumpberger, A. Mani, B. Zaltzman, and M. Z. Bazant, Overlimiting current and shock electro dialysis in porous media, *Langmuir* **29**, 16167 (2013).
- [16] D. Deng, W. Aouad, W. A. Braff, S. Schlumpberger, M. E. Suss, and M. Z. Bazant, Water purification by shock electro dialysis: Deionization, filtration, separation, and disinfection, *Desalination* **357**, 77 (2015).
- [17] S. Schlumpberger, N. B. Lu, M. E. Suss, and M. Z. Bazant, Scalable and continuous water deionization by shock electro dialysis, *Environ. Sci. Technol. Lett.* **2**, 367 (2015).
- [18] K. M. Conforti and M. Z. Bazant, Continuous ion-selective separations by shock electro dialysis, *AIChE J.* **66**, e16751 (2020).
- [19] M. A. Alkhadra, K. M. Conforti, T. Gao, H. Tian, and M. Z. Bazant, Continuous separation of radionuclides from contaminated water by shock electro dialysis, *Environ. Sci. Technol.* **54**, 527 (2019).
- [20] M. A. Alkhadra, T. Gao, K. M. Conforti, H. Tian, and M. Z. Bazant, Small-scale desalination of seawater by shock electro dialysis, *Desalination* **476**, 114219 (2020).
- [21] G. M. Homsy, Viscous fingering in porous media, *Annu. Rev. Fluid Mech.* **19**, 271 (1987).
- [22] R. Lenormand, E. Touboul, and C. Zarcone, Numerical models and experiments on immiscible displacements in porous media, *J. Fluid Mech.* **189**, 165 (1988).
- [23] M. A. Amooie, M. R. Soltanian, and J. Moortgat, Hydrothermodynamic mixing of fluids across phases in porous media, *Geophys. Res. Lett.* **44**, 3624 (2017).
- [24] C. I. Steefel, D. J. DePaolo, and P. C. Lichtner, Reactive transport modeling: An essential tool and a new research approach for the earth sciences, *Earth Planet. Sci. Lett.* **240**, 539 (2005).
- [25] M. Dentz, T. Le Borgne, A. Englert, and B. Bijeljic, Mixing, spreading and reaction in heterogeneous media: A brief review, *J. Contam. Hydrol.* **120-121**, 1 (2011).
- [26] M. A. Amooie, M. R. Soltanian, and J. Moortgat, Solutal convection in porous media: Comparison between boundary conditions of constant concentration and constant flux, *Phys. Rev. E* **98**, 033118 (2018).
- [27] S. Mahmoodpour, B. Rostami, M. R. Soltanian, and M. A. Amooie, Convective Dissolution of Carbon Dioxide in Deep Saline Aquifers: Insights from Engineering a High-Pressure Porous Visual Cell, *Phys. Rev. Applied* **12**, 034016 (2019).
- [28] A. D. Stroock, S. K. Dertinger, G. M. Whitesides, and A. Ajdari, Patterning flows using grooved surfaces, *Anal. Chem.* **74**, 5306 (2002).
- [29] A. D. Stroock, S. K. Dertinger, A. Ajdari, I. Mezić, H. A. Stone, and G. M. Whitesides, Chaotic mixer for microchannels, *Science* **295**, 647 (2002).
- [30] T. T. Al-Housseiny, P. A. Tsai, and H. A. Stone, Control of interfacial instabilities using flow geometry, *Nat. Phys.* **8**, 747 (2012).
- [31] H. S. Rabbani, D. Or, Y. Liu, C.-Y. Lai, N. B. Lu, S. S. Datta, H. A. Stone, and N. Shokri, Suppressing viscous fingering in structured porous media, *Proc. Natl. Acad. Sci. USA* **115**, 4833 (2018).
- [32] R. J. Hunter, *Zeta Potential in Colloid Science: Principles and Applications*, Vol. 2 (Academic Press, San Diego, CA, 2013).
- [33] D. Long and A. Ajdari, A note on the screening of hydrodynamic interactions, in electrophoresis, and in porous media, *Eur. Phys. J. E* **4**, 29 (2001).
- [34] M. Schmuck and M. Z. Bazant, Homogenization of the Poisson-Nernst-Planck equations for ion transport in charged porous media, *SIAM J. Appl. Math.* **75**, 1369 (2015).
- [35] E. B. Cummings, S. K. Griffiths, and R. H. Nilson, Irrotationality of uniform electro-osmosis, in *Microfluidic Devices and Systems II*, Vol. 3877 (International Society for Optics and Photonics, Bellingham, WA, 1999), pp. 180–189.

- [36] E. B. Cummings, S. Griffiths, R. Nilson, and P. Paul, Conditions for similitude between the fluid velocity and electric field in electroosmotic flow, *Anal. Chem.* **72**, 2526 (2000).
- [37] A. P. Shapiro and R. F. Probstein, Removal of contaminants from saturated clay by electroosmosis, *Environ. Sci. Technol.* **27**, 283 (1993).
- [38] R. F. Probstein and R. E. Hicks, Removal of contaminants from soils by electric fields, *Science* **260**, 498 (1993).
- [39] Y. B. Acar and A. N. Alshawabkeh, Principles of electrokinetic remediation, *Environ. Sci. Technol.* **27**, 2638 (1993).
- [40] A. N. Alshawabkeh and Y. B. Acar, Electrokinetic remediation. II: Theoretical model, *J. Geotech. Eng.* **122**, 186 (1996).
- [41] J. Virkutyte, M. Sillanpää, and P. Latostenmaa, Electrokinetic soil remediation-critical overview, *Sci. Total Environ.* **289**, 97 (2002).
- [42] S.-Y. Kim, J. H. Cho, E. Murray, N. Bakh, H. Choi, K. Ohn, L. Ruelas, A. Hubbert, M. McCue, S. L. Vassallo *et al.*, Stochastic electrotransport selectively enhances the transport of highly electromobile molecules, *Proc. Natl. Acad. Sci. USA* **112**, E6274 (2015).
- [43] E. Murray, J. H. Cho, D. Goodwin, T. Ku, J. Swaney, S.-Y. Kim, H. Choi, Y.-G. Park, J.-Y. Park, A. Hubbert *et al.*, Simple, scalable proteomic imaging for high-dimensional profiling of intact systems, *Cell* **163**, 1500 (2015).
- [44] T. Ku, J. Swaney, J.-Y. Park, A. Albanese, E. Murray, J. H. Cho, Y.-G. Park, V. Mangena, J. Chen, and K. Chung, Multiplexed and scalable super-resolution imaging of three-dimensional protein localization in size-adjustable tissues, *Nat. Biotechnol.* **34**, 973 (2016).
- [45] T. Mano, A. Albanese, H.-U. Dodt, A. Erturk, V. Gradinaru, J. B. Treweek, A. Miyawaki, K. Chung, and H. R. Ueda, Whole-brain analysis of cells and circuits by tissue clearing and light-sheet microscopy, *J. Neurosci.* **38**, 9330 (2018).
- [46] F. A. Morrison Jr., Electrophoresis of a particle of arbitrary shape, *J. Colloid Interface Sci.* **34**, 210 (1970).
- [47] C. J. v. Oss, The influence of the size and shape of molecules and particles on their electrophoretic mobility, *Sep. Purif. Methods* **4**, 167 (1975).
- [48] M. Teubner, The motion of charged colloidal particles in electric fields, *J. Chem. Phys.* **76**, 5564 (1982).
- [49] J. L. Anderson, Colloid transport by interfacial forces, *Annu. Rev. Fluid Mech.* **21**, 61 (1989).
- [50] D. Long and A. Ajdari, Symmetry Properties of the Electrophoretic Motion of Patterned Colloidal Particles, *Phys. Rev. Lett.* **81**, 1529 (1998).
- [51] D. Long and A. Ajdari, Electrophoretic mobility of composite objects in free solution: Application to dna separation, *Electrophoresis* **17**, 1161 (1996).
- [52] M. Z. Bazant and T. M. Squires, Induced-Charge Electrokinetic Phenomena: Theory and Microfluidic Applications, *Phys. Rev. Lett.* **92**, 066101 (2004).
- [53] T. M. Squires and M. Z. Bazant, Breaking symmetries in induced-charge electro-osmosis and electrophoresis, *J. Fluid Mech.* **560**, 65 (2006).
- [54] A. Ajdari, Electro-Osmosis on Inhomogeneously Charged Surfaces, *Phys. Rev. Lett.* **75**, 755 (1995).
- [55] A. Ajdari, Pumping liquids using asymmetric electrode arrays, *Phys. Rev. E* **61**, R45 (2000).
- [56] A. D. Stroock, M. Weck, D. T. Chiu, W. T. S. Huck, P. J. A. Kenis, R. F. Ismagilov, and G. M. Whitesides, Patterning Electro-Osmotic Flow with Patterned Surface Charge, *Phys. Rev. Lett.* **84**, 3314 (2000).
- [57] D. Long, H. A. Stone, and A. Ajdari, Electroosmotic flows created by surface defects in capillary electrophoresis, *J. Colloid Interface Sci.* **212**, 338 (1999).
- [58] E. Boyko, S. Rubin, A. D. Gat, and M. Bercovici, Flow patterning in Hele-Shaw configurations using non-uniform electro-osmotic slip, *Phys. Fluids* **27**, 102001 (2015).
- [59] F. Paratore, V. Bacheva, G. V. Kaigala, and M. Bercovici, Dynamic microscale flow patterning using electrical modulation of zeta potential, *Proc. Natl. Acad. Sci. USA* **116**, 10258 (2019).
- [60] F. Paratore, E. Boyko, G. V. Kaigala, and M. Bercovici, Electroosmotic Flow Dipole: Experimental Observation and Flow Field Patterning, *Phys. Rev. Lett.* **122**, 224502 (2019).
- [61] S. Alizadeh, M. Z. Bazant, and A. Mani, Impact of network heterogeneity on electrokinetic transport in porous media, *J. Colloid Interface Sci.* **553**, 451 (2019).

- [62] B. J. Kirby and E. F. Hasselbrink Jr., Zeta potential of microfluidic substrates: 1. Theory, experimental techniques, and effects on separations, *Electrophoresis* **25**, 187 (2004).
- [63] S. Y. Park, C. J. Russo, D. Branton, and H. A. Stone, Eddies in a bottleneck: An arbitrary Debye length theory for capillary electroosmosis, *J. Colloid Interface Sci.* **297**, 832 (2006).
- [64] J. P. Urbanski, T. Thorsen, J. A. Levitan, and M. Z. Bazant, Fast ac electro-osmotic micropumps with nonplanar electrodes, *Appl. Phys. Lett.* **89**, 143508 (2006).
- [65] M. Z. Bazant and Y. Ben, Theoretical prediction of fast 3D ac electro-osmotic pumps, *Lab on a Chip* **6**, 1455 (2006).
- [66] C.-C. Huang, M. Z. Bazant, and T. Thorsen, Ultrafast High-Pressure ac Electro-Osmotic Pumps for Portable Biomedical Microfluidics, *Lab on a Chip* **10**, 80 (2010).
- [67] J.-D. Chen and D. Wilkinson, Pore-Scale Viscous Fingering in Porous Media, *Phys. Rev. Lett.* **55**, 1892 (1985).
- [68] R. Holtzman, Effects of pore-scale disorder on fluid displacement in partially wettable porous media, *Sci. Rep.* **6**, 36221 (2016).
- [69] M. Mirzadeh, F. Gibou, and T. M. Squires, Enhanced Charging Kinetics of Porous Electrodes: Surface Conduction as a Short-Circuit Mechanism, *Phys. Rev. Lett.* **113**, 097701 (2014).
- [70] S. Alizadeh and A. Mani, Multiscale model for electrokinetic transport in networks of pores, Part I: Model derivation, *Langmuir* **33**, 6205 (2017).
- [71] Z. Gu and M. Z. Bazant, Microscopic theory of capillary pressure hysteresis based on pore-space accessibility and radius-resolved saturation, *Chem. Eng. Sci.* **196**, 225 (2019).
- [72] E. Brunet and A. Ajdari, Generalized onsager relations for electrokinetic effects in anisotropic and heterogeneous geometries, *Phys. Rev. E* **69**, 016306 (2004).
- [73] P. Mazur and J. T. G. Overbeek, On electro-osmosis and streaming-potentials in diaphragms: II. General quantitative relationship between electro-kinetic effects, *Recl. Trav. Chim.* **70**, 83 (1951).
- [74] R. O'Brien, Electroosmosis in porous materials, *J. Colloid Interface Sci.* **110**, 477 (1986).
- [75] E. Petersen, Diffusion in a pore of varying cross section, *AIChE J.* **4**, 343 (1958).
- [76] T. R. Ferguson and M. Z. Bazant, Nonequilibrium thermodynamics of porous electrodes, *J. Electrochem. Soc.* **159**, A1967 (2012).
- [77] G. E. Archie *et al.*, The electrical resistivity log as an aid in determining some reservoir characteristics, *Trans. AIME* **146**, 54 (1942).
- [78] F. H. Van der Heyden, D. J. Bonhuis, D. Stein, C. Meyer, and C. Dekker, Electrokinetic energy conversion efficiency in nanofluidic channels, *Nano Lett.* **6**, 2232 (2006).
- [79] M. Shinozuka and C.-M. Jan, Digital simulation of random processes and its applications, *J. Sound Vib.* **25**, 111 (1972).
- [80] M. Shinozuka and G. Deodatis, Simulation of stochastic processes by spectral representation, *Appl. Mech. Rev.* **44**, 191 (1991).
- [81] W. R. Sill, Self-potential modeling from primary flows, *Geophysics* **48**, 76 (1983).
- [82] P. W. Glover, E. Walker, and M. D. Jackson, Streaming-potential coefficient of reservoir rock: A theoretical model, *Geophysics* **77**, D17 (2012).
- [83] J. Dunkel, S. Heidenreich, K. Drescher, H. H. Wensink, M. Bär, and R. E. Goldstein, Fluid Dynamics of Bacterial Turbulence, *Phys. Rev. Lett.* **110**, 228102 (2013).
- [84] A. Levy, M. McEldrew, and M. Z. Bazant, Spin-glass charge ordering in ionic liquids, *Phys. Rev. Materials* **3**, 055606 (2019).
- [85] C. Nicolaidis, B. Jha, L. Cueto-Felgueroso, and R. Juanes, Impact of viscous fingering and permeability heterogeneity on fluid mixing in porous media, *Water Resour. Res.* **51**, 2634 (2015).
- [86] T. Le Borgne, M. Dentz, and E. Villermaux, Stretching, Coalescence, and Mixing in Porous Media, *Phys. Rev. Lett.* **110**, 204501 (2013).
- [87] M. A. Amooie, M. R. Soltanian, F. Xiong, Z. Dai, and J. Moortgat, Mixing and spreading of multiphase fluids in heterogeneous bimodal porous media, *Geomech. Geophys. Geo-Energy Geo-Resour.* **3**, 225 (2017).
- [88] J. D. Posner and J. G. Santiago, Convective instability of electrokinetic flows in a cross-shaped microchannel, *J. Fluid Mech.* **555**, 1 (2006).

- [89] J. D. Posner, C. L. Pérez, and J. G. Santiago, Electric fields yield chaos in microflows, *Proc. Natl. Acad. Sci. USA* **109**, 14353 (2012).
- [90] I. Rubinstein and B. Zaltzman, Electro-osmotically induced convection at a permselective membrane, *Phys. Rev. E* **62**, 2238 (2000).
- [91] B. Zaltzman and I. Rubinstein, Electro-osmotic slip and electroconvective instability, *J. Fluid Mech.* **579**, 173 (2007).
- [92] C. Druzgalski, M. Andersen, and A. Mani, Direct numerical simulation of electroconvective instability and hydrodynamic chaos near an ion-selective surface, *Phys. Fluids* **25**, 110804 (2013).
- [93] See Supplemental Material at <http://link.aps.org/supplemental/10.1103/PhysRevFluids.5.103701> for an animated simulation.